Electronic Journal of Biotechnology 73 (2025) 18–31

Contents lists available at ScienceDirect

Electronic Journal of Biotechnology

journal homepage: www.elsevier.com/locate/ejbt

Research article

# Antibiotic evaluation of the nanocomposites IONs-MWCNTs-Pc and IONs-GO-Pc encapsulated in the biocompatible hydrogel poly(VCL-co-PEGDA) based on photodynamic effect ☆

Coralia Cuadrado [a,*], Alex Mantilla [b], Luis Hidalgo [a], Diego Punina [a]

[a] Facultad de Mecánica, Escuela Superior Politécnica de Chimborazo, Panamericana Sur km 1 1/2, Riobamba, 060155, Ecuador
[b] Facultad de Administración de Empresas, Escuela Superior Politécnica de Chimborazo, Panamericana Sur km 1 1/2, Riobamba, 060155, Ecuador

## GRAPHICAL ABSTRACT

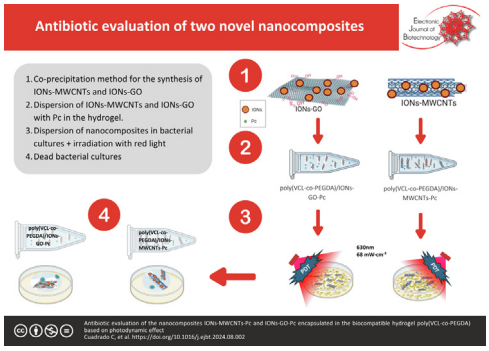


Antibiotic evaluation of two novel nanocomposites.

## ARTICLE INFO

*Article history:*
Received 22 May 2024
Accepted 13 August 2024
Available online 18 October 2024

*Keywords:*
Antibiotic evaluation
Antibiotic-resistant bacteria
Antimicrobial
Biocompatible hydrogel matrix
Carbon nanotubes
Graphene oxide
Drug delivery
Hydrogels
Iron Oxide Nanoparticles

## ABSTRACT

*Background:* The rise of drug-resistant bacteria, including *Staphylococcus aureus* and *Escherichia coli*, presents a significant healthcare challenge. This study focuses on the development of two novel nanocomposites IONs-MWCNTs-Pc and IONs-GO-Pc encapsulated within a biocompatible poly(VCL-co-PEGDA) hydrogel. These composites are designed for use in photodynamic therapy and evaluated for their antimicrobial efficacy against resistant pathogens.

*Results:* The synthesized nanocomposites, when irradiated with red light at 630 nm, showed significant antimicrobial activity, resulting in a marked reduction in the viability of *S. aureus* ATCC 27543, *S. aureus* ATCC 33591, and *E. coli* ATCC 971182. Photodynamic studies demonstrated that the IONs-GO-Pc nanocomposite was more efficient in generating singlet oxygen compared to IONs-MWCNTs-Pc, which correlated with its superior antimicrobial performance. Structural and chemical characterization confirmed the successful incorporation of nanomaterials and photosensitizers, enhancing the photodynamic effect.

*Conclusions:* The study demonstrates that both IONs-MWCNTs-Pc and IONs-GO-Pc nanocomposites show promise as alternative treatments for infections caused by antibiotic-resistant bacteria, with the GO-

☆ Audio abstract available in Supplementary material.

* Corresponding author.
*E-mail address:* coralia.cuadrado@espoch.edu.ec (C. Cuadrado).

https://doi.org/10.1016/j.ejbt.2024.08.002

Nanocomposites
Photodynamic effect

based composite showing higher photodynamic therapy efficacy. These findings suggest that such nanocomposites could play a pivotal role in advancing antimicrobial strategies against resistant pathogens.
**How to cite:** Cuadrado C, Mantilla A, Hidalgo L, et al. Antibiotic evaluation of the nanocomposites IONs-MWCNTs-Pc and IONs-GO-Pc encapsulated in the biocompatible hydrogel poly(VCL-co-PEGDA) based on photodynamic effect. Electron J Biotechnol 2025;73. https://doi.org/10.1016/j.ejbt.2024.08.002.


## 1. Introduction

The World Health Organization (WHO) has identified microbial diseases as one of the primary threats to human health due to their rapid growth and spread across various environments [1]. To combat infectious diseases caused by pathogens such as *Escherichia coli*, *Staphylococcus aureus*, and *Klebsiella pneumoniae*, among others, various antibiotic therapies have been developed; however, these therapies have been losing their efficacy [2]. The loss of antibiotic efficacy is attributed to microorganisms developing new mechanisms to adapt and grow in the presence of antibiotics that previously eliminated them, resulting in resistance to commonly used antibiotics [3,4]. Therefore, the development of new antimicrobial treatments that are effective and readily accessible is necessary [4].

An alternative tool in the fight against pathogenic microorganisms is the use of nanotechnology to develop nanocomposites capable of eliminating various types of microorganisms [5,6]. The use of nanomaterials in phototherapies, such as Photodynamic Therapy (PDT) and Photothermal Therapy (PTT), has achieved significant effectiveness in eliminating microorganisms due to their selectivity, minimal invasiveness, high specificity, and low risk of developing drug resistance [7,8].

Carbon-based nanomaterials such as graphene oxide (GO), fullerenes (C60), carbon nanotubes (CNTs) including multi-walled carbon nanotubes (MWCNTs) and single-walled carbon nanotubes (SWCNTs), carbon dots (CDs), and nanodiamonds (NDs) are widely used in antimicrobial applications. These can be modified or functionalized with other compounds or nanoparticles to enhance their solubility, biocompatibility, and drug-loading capacity [9–11]. Additionally, they can be combined in phototherapies to improve their efficacy.

Microorganism photoinactivation based on the PDT technique is achieved through the interaction of three important elements: light, photosensitizer (PS), and molecular oxygen, which, when combined in appropriate doses, generate reactive oxygen species (ROS). The generation of ROS increases microorganism permeability, causes physical damage to the membrane, and damages proteins, lipids, and DNA, ultimately leading to bacterial death [12,13].

Over the past five decades, magnetic nanoparticles (MNPs) have been studied due to their unique physicochemical properties, intrinsic magnetic nature, chemical stability, biocompatibility, and low-cost production [14]. MNPs have been widely used in biomedicine for applications such as cell therapy, hyperthermia, magnetic separation, magnetic resonance imaging, biomolecule sensors, drug delivery, cancer treatment and diagnosis (theranostics), and antimicrobial agents, among others [15,16,17].

Iron oxide nanoparticles (IONs), such as magnetite, maghemite, and hematite, are obtained from iron oxides and are widely used in biomedicine due to their biocompatibility and lack of cytotoxicity at concentrations below 100 $\mu g \cdot mL^{-1}$ [18]. Currently, an important use of IONs is their antimicrobial application, as they can act as antimicrobial agents or synergize with other antimicrobial agents, nanostructures, and phototherapies [15,16].

A crucial characteristic of photosensitizers and nanomaterials for biological applications is their complete dispersion in an aqueous medium [6,19]. To achieve this, surfactants, pH adjustment, co-solvents like ethanol, methanol, or dimethyl sulfoxide (DMSO), and dispersion in hydrogels are used [20,21]. Obtaining a nanomaterial dispersed in an aqueous solution enhances its stability, biocompatibility, and bioactivity [22,23,24]. In this research, the biocompatible hydrogel poly(N-vinyl caprolactam-co-poly(ethylene glycol) diacrylate) (poly(VCL-co-PEGDA)) is used, abbreviated as poly (VCL-co-PEGDA), which has a lower critical solution temperature (LCST) of 32°C and is used for drug delivery, releasing 68% of the drug at 38°C after 24 h according to Romero et al. [25].

This study aims to develop the nanocomposites: poly(VCL-co-PEGDA)/IONs-MWCNTs-Pc and poly(VCL-co-PEGDA)/IONs-GO-Pc. Their physical and chemical properties will be evaluated using FT-IR spectroscopy, Raman spectroscopy, UV–VIS spectroscopy, magnetization (M), X-ray diffraction (XRD), scanning electron microscopy (SEM), energy-dispersive X-ray spectroscopy (EDS), and transmission electron microscopy (TEM). The antimicrobial properties based on PDT phototherapy of the two compounds will be evaluated in the bacteria: *S. aureus* ATCC: 27543 (*S. aureus 1*), methicillin-resistant *S. aureus* ATCC: 33591 (*S. aureus 2*) and *E. coli* ATCC: 971182.

## 2. Materials and methods

### 2.1. Materials

The MWCNTs, GO, and the photosensitizer Zinc Phthalocyanine-Menthol were sourced from PUC-RIO and the University of São Carlos, Brazil. The reagents used for the synthesis of the nanocomposites poly(VCL-co-PEGDA)/IONS-MWCNTs-Pc and poly(VCL-co-PEGDA)/IONS-GO-Pc were $Fe_2(SO_4)_3 \cdot H_2O$ (Baker's Analyzed, USA); sodium dodecyl sulfate emulsifier (SDS, STEOL®CS-230 from Stepan Company, USA); $Fe(SO_4)$, $H_2SO_4 \cdot 7H_2O$ (MERCK, Germany); $HNO_3$ (Fermont, Mexico); ammonium persulfate initiator (APS, > 99%, from FMC Corporation, USA); $NH_4OH$, 14.8 N, and N,N-dimethylformamide (Fisher Scientific, USA); N-vinylcaprolactam (VCL, 98%), poly(ethylene glycol) diacrylate (PEGDA, Mn 250 $g \cdot mol^{-1}$), and sodium hydrogen carbonate buffer ($CHNaO_3$, $\geq$ 99.7%) from Sigma Aldrich, Germany; saline solution (Fisiol UB pH = 7 from Lamosan, Ecuador); Tween80 (La casa del Químico, Ecuador), and for the antimicrobial study, the microorganisms used were *S. aureus* ATCC: 27543, *S. aureus* ATCC: 33591 and *E. coli* ATCC: 971182.

The characterization of the IONs-MWCNTs and IONs-GO nanocomposites was conducted using spectroscopy techniques. A JASCO FT/IR-4100 spectrometer was utilized for FT-IR analysis, with a resolution of 0.7 $cm^{-1}$, covering a wavenumber range from 7800 to 350 $cm^{-1}$. Additionally, Raman analyses were performed using a HORIBA LabRAM HR Evolution spectrometer, with sample excitation at 2.33 eV (532 nm). To assess the temporal stability of the photosensitizer (PS) in the nanocomposites, UV–VIS spectroscopy was employed, conducting analyses with a Thermo Fisher Scientific Evolution 220 spectrophotometer, operating with a resolution greater than 1.8 Å, in a range from 280 to 780 nm. Finally, X-ray diffraction (XRD) analyses were performed using a PANalytical

EMPYREAN diffractometer. This instrument was configured in the θ-2θ mode (Bragg-Brentano geometry) and is equipped with a copper X-ray tube (Kα radiation, λ = 1.54056 Å), operating at 45 kV and 40 mA.

Photothermal and photodynamic analyses were conducted using laboratory-adapted equipment, including a red-light LED lamp at 635 nm and 68 $mW{\cdot}cm^{-2}$. For the photodynamic analyses, a substrate sensitive to singlet oxygen ($^1O_2$) was used to measure the ability of the nanocomposites to generate $^1O_2$. The decrease in DPBF absorbance will be observed using a UV–VIS spectrophotometer, the Specord 210 Plus, which has a resolution of 2.3–2.5 nm. Regarding the magnetic properties, magnetization (M) measurements were carried out using a Quantum Design Versalab vibrating sample magnetometer (VSM), within a temperature range of −210 to +60°C and with magnetic fields of up to 3 T.

The analysis of antimicrobial activity was conducted using strains of microorganisms, including *S. aureus 1, S. aureus 2* and *E. coli*. For the cultures, Mueller-Hinton agar from Difco™ was used, incubating them at a constant temperature of 37°C. Measurements were performed using a Thermo Scientific™ Orion™ AquaMate 8000 UV–Vis spectrophotometer and 1.5 mL microtubes.

For structural characterization, a Tescan Mira 3 scanning electron microscope (SEM) was utilized, equipped with a Schottky field emitter and a Bruker X-Flash 6–30 detector, achieving a resolution of 123 eV in Mn Kα for energy dispersive X-ray spectroscopy (EDS). Additionally, a Bruker Dimension Icon atomic force microscope (AFM) and a FEI Tecnai G2 Spirit Twin transmission electron microscope (TEM) were used, equipped with an Eagle 4 k HR camera at 80 kV and a TEM grid of formvar/carbon with a 300 mesh.

## 2.2. Methods

### 2.2.1. Synthesis of IONs-MWCNTs and IONs-GO

Initially, the purification of MWCNTs was carried out through an acidification process. For this purpose, 5.3 mg of MWCNTs were dispersed in 10 mL of distilled water containing 5% of the surfactant Tween 80, and this mixture was stirred at 200 rpm for 24 h. Subsequently, 4 mL of nitric acid was mixed with 12 mL of sulfuric acid in a ratio of 1:3. This acidic solution was then carefully added to the MWCNTs suspension under magnetic stirring at the same speed. The final pH adjustment of the MWCNTs solution was achieved through successive washings and filtration using a microporous filter of 0.22 μm.

The synthesis of IONs in the presence of MWCNTs and GO was carried out using the coprecipitation method. In the procedure, 5.3 mg of purified MWCNTs, 225 mg of $FeSO_4$, and 450 mg of $Fe_2(SO_4)_3$ were dispersed along with 5% Tween 80 in 18 mL of distilled water. This mixture was stirred magnetically for 3 h. Subsequently, it was carefully added to 150 mL of $NH_4OH$, maintaining stirring in an inert atmosphere at 200 rpm for one hour. After this, several magnetic purifications of the IONs-MWCNTs nanocomposite were performed until a neutral pH was reached. Finally, the solution was dried in an oven at 40°C to obtain a solid. For the IONs-GO nanocomposite, the same method was replicated, substituting MWCNTs with 5.3 mg of GO. As a control, IONs were synthesized without adding GO or MWCNTs, using the same coprecipitation process. The final ratio of IONs to MWCNTs and IONs to GO in the nanocomposites was determined to be approximately 26.91:1.

### 2.2.2. Synthesis of hydrogel

The preparation of the hydrogel was conducted through emulsion polymerization in a flat-bottomed flask that was coupled to a reflux condenser. Initially, 235 mL of deionized water was introduced into the flask, to which a dispersion of 2 g of VCL (monomer), 0.08 g of PEGDA (crosslinking agent), 0.08 g of SDS-STEOL CS-230 (emulsifying agent), and 0.08 g of $NaHCO_3$ (buffering agent) was added. This mixture was stirred at 350 rpm and heated to 70°C under a nitrogen atmosphere for one hour. Subsequently, the initiator APS (0.03 g dissolved in 15 mL of distilled water) was incorporated into the solution, continuing the reaction at the same temperature for another seven hours. At the end of this period, the mixture was cooled to 25°C while stirring at 200 rpm for 12 h to prevent aggregation. The process concluded with the dialysis of the hydrogel against DDI water (1.7 μS) to remove any impurities or residual reactants [26].

### 2.2.3. Dispersion of IONs-MWCNTs and IONs-GO with Pc in the hydrogel

The dispersion of the IONs-MWCNTs and IONs-GO nanocomposites with Pc in the poly(VCL-co-PEGDA) hydrogel began by dispersing 2 mg of IONs-MWCNTs in 10 mL of distilled water with 5% Tween 80. This mixture was magnetically stirred at 200 rpm for 24 h and then subjected to ultrasound for 30 min. To this solution, 10 mL of poly(VCL-co-PEGDA) was added, resulting in a final concentration of 100 $\mu g{\cdot}mL^{-1}$ (MWCNTs = 3.47 $\mu g{\cdot}mL^{-1}$, IONs = 93.3 $\mu g{\cdot}mL^{-1}$, and Pc = 8.1 μM) for IONs-MWCNTs, and it was magnetically stirred for four hours at the same speed to form the poly(VCL-co-PEGDA)/IONs-MWCNTs nanocomposite. To incorporate the photosensitizer Pc, 0.67 mL of Pc (0.25 mM) was mixed with 20 mL of the poly(VCL-co-PEGDA)/IONs-MWCNTs nanocomposite, and the mixture was exposed to ultrasound for 4 h at 250 rpm and 23°C, resulting in the poly(VCL-co-PEGDA)/IONs-MWCNTs-Pc nanocomposite (sample 1). The same method was applied to obtain the poly(VCL-co-PEGDA)/IONs-GO-Pc nanocomposite (sample 2), substituting IONs-MWCNTs with IONs-GO, yielding a final concentration of 100 $\mu g{\cdot}mL^{-1}$ (GO = 3.47 $\mu g{\cdot}mL^{-1}$, IONs = 93.3 $\mu g{\cdot}mL^{-1}$, and Pc = 8.1 μM) for IONs-GO after the addition of VCL/PEGDA.

### 2.2.4. Optical, photodynamic, photothermal, and magnetic studies of the nanocomposites

For the study of optical properties, the following samples were prepared: Pc-DMF, poly(VCL-co-PEGDA)/Pc, poly(VCL-co-PEGDA)/IONs-MWCNTs-Pc, and poly(VCL-co-PEGDA)/IONs-GO (Pc = 8.1 μM, GO 3.47 $\mu g{\cdot}mL^{-1}$, MWCNTs = 3.47 $\mu g{\cdot}mL^{-1}$). These were analyzed at different times over 24 h using a UV–VIS SPECORD 210 Plus spectrophotometer in a range of 300 to 800 nm. For each measurement, the samples were stored in darkness to prevent photodegradation of the composite and thus evaluate the percentage of Pc release.

For the photodynamic study, the photobleaching test of the substrate 1,3-diphenylisobenzofuran (DPBF) was carried out. An initial solution was prepared by dispersing 5 mg of DPBF in 1 mL of N, N-Dimethylformamide (DMF). Aliquots of this solution were then taken and added to solutions of: poly(VCL-co-PEGDA)/IONs-MWCNTs, poly(VCL-co-PEGDA)/IONs-GO, sample 1 and sample 2. The selection of these nanocomposites was based on the ability of carbon-based materials and photosensitizers (PS) to induce photodynamic effects when exposed to specific wavelengths [27,28].

Photothermal analyses were conducted using DDI water (1.7 μS), poly(VCL-co-PEGDA), IONs, MWCNTs, GO, sample 1 and sample 2. The purpose of these studies was to investigate the photothermal effect of each of the components present in the samples 1 and 2. To conduct these studies, 1 mL of the nanocomposite under study was introduced into a 1 mL cuvette. Subsequently, the sample was irradiated with red light at 630 nm and

an intensity of 68 mW·cm$^{-2}$ for variable periods, monitoring the temperature every 5 to 10 min until thermal stabilization was observed.

To evaluate, if the incorporation of the nanocomposites in the hydrogel affects their magnetic properties, magnetization curves as a function of the applied magnetic field ($\vec{M}$ vs $\vec{H}$) were measured using a Quantum Design Versalab vibrating sample magnetometer (VSM), with applied magnetic fields ($\mu_0 H$) ranging from −3 to 3 T and a sensitivity of approximately ∼ 1x10$^{-6}$ emu. Powder samples of poly(VCL-co-PEGDA)/IONs-MWCNTs-Pc and poly(VCL-co-PEGDA)/IONs-GO-Pc, and as a reference, IONs, were used. To analyze the magnetic behavior and the coercive field of the samples, temperatures of −210°C and +60°C were selected.

### 2.2.5. Antimicrobial studies

For the antimicrobial studies, cryovials containing the microorganisms under study were used: *S. aureus 1, S. aureus 2* and *E. coli*. The microorganisms were incubated overnight at 37°C in Mueller-Hinton agar. Subsequently, the absorbance of each culture was measured using a spectrophotometer, and the concentration in the Mueller-Hinton agar was adjusted to the specific concentrations for the assays, being $10^7$ CFU·mL$^{-1}$ for *E. coli* and $10^6$ CFU·mL$^{-1}$ for *S. aureus* according to the McFarland scale.

Once the concentrations were adjusted, the experiment was conducted with each microorganism. Initially, 1 mL aliquots of each microorganism were distributed into microtubes according to the layout in Table 1.

Subsequently, the microtubes were centrifuged at 3000 rpm for 10 min, discarding the supernatant and preserving the microbial pellet, to which 1 mL of PBS was added to wash and remove residues from the culture medium. This wash was centrifuged under the same conditions and the PBS was discarded, leaving only the pellet. One mL of the respective nanocomposite was added to each microtube, using sample 1 and sample 2 at a concentration of 100 μg·mL$^{-1}$ (GO = 3.47 μg·mL$^{-1}$, MWCNTs = 3.47 μg·mL$^{-1}$, IONs = 93.3 μg·mL$^{-1}$, and Pc = 8.1 μM). For the controls, the cells were resuspended in PBS. Each tube was shaken to resuspend the pellet and then incubated at 37°C in darkness for 45 min.

After incubation, the contents of each microtube designated with +light were irradiated with red light at 630 nm. The remaining microtubes (+dark) did not receive irradiation. Subsequently, serial dilutions in PBS were made for each sample, inoculating 4 μL of each dilution onto an octopartite Petri dish with Mueller-Hinton agar. Each inoculum was spread to isolate colonies, and the plates were incubated at 37°C for 24 h, after which the colonies formed in each dilution were counted. Each experiment was repeated in triplicate.

### 2.2.6. Morphology and elemental characterizations

The morphology and elemental composition of the nanomaterials: IONs, MWCNTs, GO, IONs-MWCNTs, IONs-GO, sample 1, and sample 2. They were evaluated using SEM and EDS. For the SEM measurements, a sample was placed on an aluminum holder using double-sided carbon tape and examined with a Tescan Mira 3 SEM. The EDS measurements were carried out within the same SEM chamber using a Bruker detector. Additionally, AFM in Tapping mode was used to assess the morphology and thickness of GO.

For TEM, samples of the nanocomposites were dispersed in a BRANSON 1510 ultrasonic bath for 30 min. Subsequently, about 5 μL of the dispersion was applied to a TEM grid coated with formvar and carbon (mesh 300), and excess solvent was removed with filter paper. Observations were made using a FEI Tecnai G2 Spirit Twin TEM, equipped with an Eagle 4 k HR camera operating at 80 kV.

**Table 1**
Aliquots distribution.

| | | | |
|---|---|---|---|
| 1 | ***E. coli* + dark (control)** | ***S. aureus 1* + dark (control)** | ***S. aureus 2* + dark (control)** |
| 2 | *E. coli* + ligh (control) | *S. aureus 1* + ligh (control) | *S. aureus 2* + ligh (control) |
| 3 | *E. coli* + Sample 1 + dark | *S. aureus 1* + Sample 1 + dark | *S. aureus 2* + Sample 1 + dark |
| 4 | *E. coli* + Sample 1 + light | *S. aureus 1* + Sample 1 + light | *S. aureus 2* + Sample 1 + light |
| 5 | *E. coli* + Sample 2 + dark | *S. aureus 1* + Sample 2 + dark | *S. aureus 2* + Sample 2 + dark |
| 6 | *E. coli* + Sample 2 + light | *S. aureus 1* + Sample 2 + light | *S. aureus 2* + Sample 2 + light |

## 3. Results and Discussion

### 3.1. Composition and structural characterization of IONs-MWCNTs and IONs-GO

FT-IR spectroscopy analysis was conducted on the magnetic nanocomposites IONs-MWCNTs and IONs-GO to study the differences in oxygen-related functional groups. Fig. 1(a) shows the FT-IR spectra of IONs-MWCNTs, which display the characteristic bands of MWCNTs and the presence of IONs. The bands around 3362 and 1340 cm$^{-1}$ correspond to the stretching and bending vibrations, respectively, of the O—H bond, revealing the presence of hydroxyl groups in the MWCNTs. The bands around 2897 and 2830 cm$^{-1}$ are due to the asymmetric and symmetric stretching of the C—H group, while the band at 876 cm$^{-1}$ is due to the bending of the C—H group. The bands appearing at 2346, 2309, and 1060 cm$^{-1}$ are primarily due to stretching associated with carbon chains. The C═O stretching band located at 1728 cm$^{-1}$ suggests that the IONs are anchored to the carboxyl groups of the MWCNTs through hydrogen bonds [29]. The bands at 1641 and 1567 cm$^{-1}$ correspond to the aromatic stretching of C═C. Finally, the characteristic bands of the IONs appear at 687 and 617 cm$^{-1}$, indicating the stretching vibration of Fe-O characteristic of IONs, which is consistent with the findings reported by Abrinaei et al. [29].

Fig. 1b presents the FT-IR spectra of the IONs-GO nanovehicle where characteristic bands of GO and IONs are identified. The bands around 3276 and 1345 cm$^{-1}$ correspond to the stretching

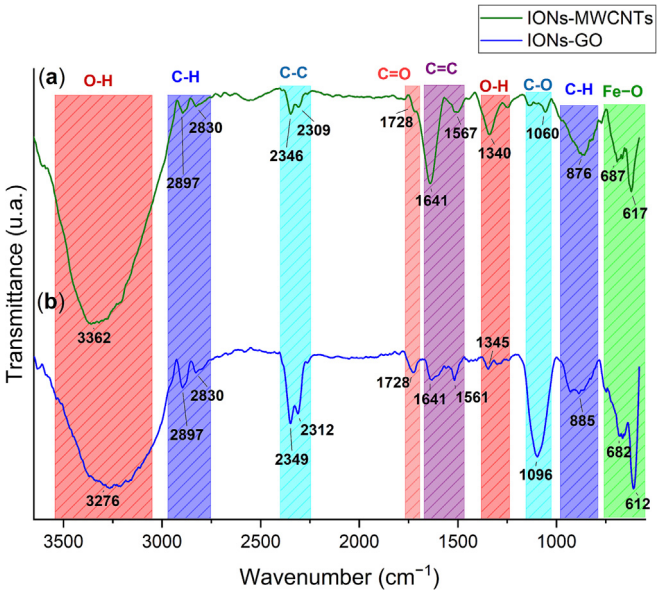


**Fig. 1. FT-IR Spectra:** (a) IONs-MWCNTs; (b) IONs-GO.

and bending vibrations, respectively, of the O—H bond, revealing the presence of hydroxyl groups in the GO. The bands around 2897 and 2830 $cm^{-1}$ are due to the asymmetric and symmetric stretching of the C—H group, while the band at 885 $cm^{-1}$ is due to the bending of the C—H group. The bands appearing at 2349, 2312, and 1096 $cm^{-1}$ are primarily due to stretching associated with carbon chains. The C═O stretching band located at 1728 $cm^{-1}$ suggests that the IONs are anchored to the carboxyl groups of GO. The bands at 1641 and 1567 $cm^{-1}$ correspond to the aromatic stretching of C═C, which is consistent with the work of Al-Ruqeishi et al. [30]. The characteristic bands of the IONs appear at 682 and 612 $cm^{-1}$ indicating the stretching vibration of Fe—O [29].

In Fig. 2, Raman spectroscopy studies of the following nanocomposites are presented: unpurified MWCNTs (Fig. 2a), purified MWCNTs (Fig. 2b), and IONs –MWCNTs (Fig. 2c). These spectra display characteristic bands of MWCNTs: the D band or defect band, and the first and second-order G and 2D bands, respectively. The D band is located at 1337 $cm^{-1}$ and indicates the presence of defects in graphite, resulting from the presence of multiple carbon sheets that are not aligned directly sheet-to-sheet, which induces a loss of translational symmetry in the two-dimensional network. Due to the same effect, a secondary phonon is produced, leading to the presence of the G band at 1566 $cm^{-1}$. The fundamental G band is a tangential stretching band attributed to the in-plane vibration of the C—C bond, typical of carbon-derived materials and consistent with literature reports [31,32,33,34].

Fig. 2d displays the Raman spectra of IONs with their characteristic bands: the $A_{1g}$ modes at 226, 502 $cm^{-1}$, $E_g$ modes at 248, 291, 300, 407, and 615 $cm^{-1}$, and the characteristic band of two-magnon scattering at 1320 $cm^{-1}$, which are consistent with the results presented by Soler and Qu [26]. Some of these bands can also be observed in the spectra shown in Fig. 2c and Fig. 2f.

The Raman spectra of not purified MWCNTs (Fig. 2a) and purified MWCNTs (Fig. 2b) show the $\frac{I_D}{I_G}$ ratio, where purified MWCNTs have a higher value $\left(\frac{I_D}{I_G} = 0.558\right)$ compared to unpurified MWCNTs $\left(\frac{I_D}{I_G} = 0.447\right)$. The increase in the $\frac{I_D}{I_G}$ ratio is due to an increase in structural defects. This may be because acid treatment causes some bonds to break and form functional groups, creating defects in the structure of the MWCNTs. Additionally, as evidenced in Fig. 2c, corresponding to the spectrum of IONs-MWCNTs, there is an increase in the $\frac{I_D}{I_G}$ ratio to 0.639, due to charge transfer effects between IONs and MWCNTs; as a result of functionalization, this indicates a MWCNTs structure with more defects. Moreover, additional bands corresponding to the IONs are observed.

Fig. 2e displays the characteristic bands of GO, including an intense D band at 1340 $cm^{-1}$, a G phase vibration band at 1589 $cm^{-1}$, and the D + D' band situated around 2900 $cm^{-1}$, which is activated by defects and appears with a combination of phonons with different linear momenta around the K and Γ points in the Brillouin zone, consistent with what was mentioned by Cançado et al. [35] and Muhammad Hafiz et al. [36]. The $\frac{I_D}{I_G}$ ratio of 1.037 results from the degree of disorder in the GO, due to the presence of carboxylic acid functional groups at its edges. Fig. 2f shows the spectra of the IONs-GO nanocomposite where a shift in the D band is observed; this is explained by the nature of the IONs, as when combined with carbon nanostructures they affect the spectral amplification of the phonon peaks, consistent with the information presented by Ramirez et al. [37] and Satheesh et al. [38].

### 3.2. Optical properties and drug delivery

UV–VIS absorbance spectra were obtained to determine if there is aggregation of the nanocomposites dispersed in hydrogel and at the same time to determine the percentage of PS release from the nanocomposites over time. In the supplementary material (**Fig. S1a,b,d** and **Fig. S2b**), Pc-DMF, poly(VCL-co-PEGDA)/Pc, poly (VCL-co-PEGDA)/IONs-MWCNTs-Pc, and poly(VCL-co-PEGDA)/ IONs-GO-Pc are presented, respectively. For all these compounds, the presence of the B or Soret band at 354 nm, a band at 616 nm, and the Q band at 684 nm, characteristic of the absorption spectra of Pc [39], are observed. Additionally, it can be seen in the figures mentioned at the beginning of the paragraph that as the concentration of Pc increases, the absorption of the 3 characteristic bands of PS (354, 616, and 684 nm) increases proportionally. This allows us to conclude that the Beer-Lambert law is fulfilled and therefore, there is no aggregation of the PS. This indicates that

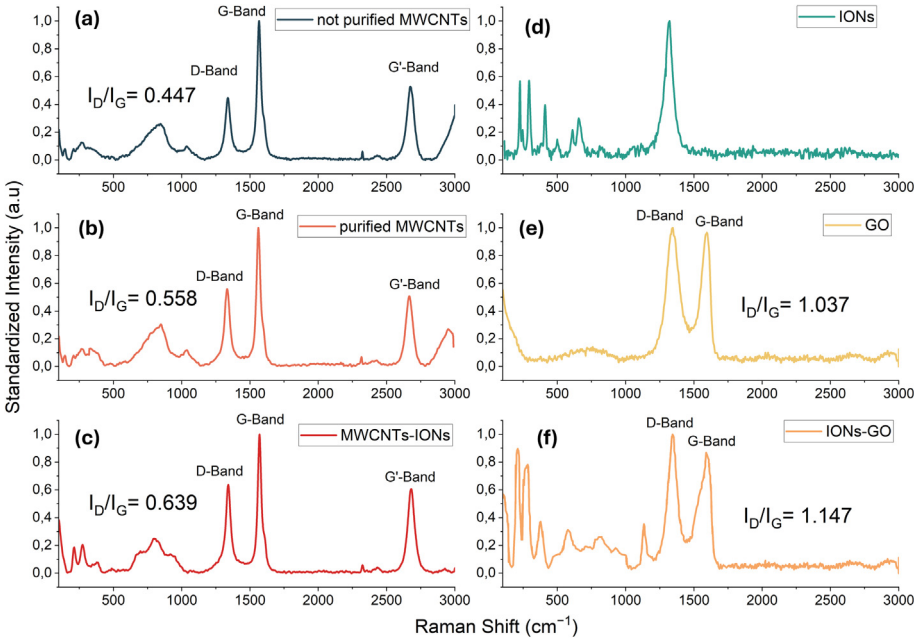


**Fig. 2. Raman Spectra:** (a) not purified MWCNTs, (b) purified MWCNTs, (c) IONs-MWCNTs; (d) IONs; (e) GO; (f) IONs-GO; Laser energy = 2.33 eV, wavelength = 532 nm.

DMF [39] and the poly(VCL-co-PEGDA) hydrogel adequately disperse the PS.

In **Fig. S1c,d** and **Fig. S2a,b** the UV–VIS spectra of poly(VCL-co-PEGDA)/IONs-MWCNTs, poly(VCL-co-PEGDA)/IONs-MWCNTs-Pc, poly(VCL-co-PEGDA)/IONs-GO, and poly(VCL-co-PEGDA)/IONs-GO-Pc are presented, respectively. Due to equipment limitations, it is not possible to observe the characteristic band of MWCNTs at 265 nm [40], nor the characteristic bands of GO at 232 nm corresponding to the $\pi \rightarrow \pi^*$ transitions of C—C aromatic bonds and the band at ~300 nm attributed to the $n \rightarrow \pi^*$ transitions of C═O bonds, as mentioned in the study by Bera et al. [41]. However, a band around 315 nm characteristic of Hematite anchored to a carbon-based structure is identified. This latter band has undergone a hypsochromic shift due to functionalization with both MWCNTs and GO in the presence of an organic solvent (ammonium hydroxide used for the synthesis of IONs, as described in the literature [42,43].

The calibration curve shown in Fig. 3 was obtained from the Q band at 684 nm of the nanocomposite poly(VCL-co-PEGDA)/IONs-GO; this band is representative of the Pc and is described in the first paragraph of this section. The Q band is located in a region of the spectra of interest for treatments based on the PDT strategy. It can be observed that the higher the concentration of Pc in the nanocomposites in Fig. 3, the higher the intensity of the 684 nm band; however, when compared with Pc dispersed in DMF, the latter shows the highest intensity relative to all the nanocomposites. This indicates that the poly(VCL-co-PEGDA) hydrogel adequately disperses the hydrophobic Pc PS in an aqueous solution, as indicated in the literature [44–46]. Additionally, it can be observed that the absorption band at 684 nm of Pc (8.1 μM) decreases as the number of functionalized components increases, these values can be seen in Table 2. The percentage of absorbance decrease of the Pc in the nanocomposites: poly(VCL-co-PEGDA)/Pc is 27.77%; poly(VCL-co-PEGDA)/IONs-MWCNTs-Pc, is 37.95%, and for the poly(VCL-co-PEGDA)/IONs-GO-Pc, it is 35.1%.

The study on the stability over time of the nanocomposites: Pc-DMF, poly(VCL-co-PEGDA)/Pc, poly(VCL-co-PEGDA)/IONs-MWCNTs-Pc, and poly(VCL-co-PEGDA)/IONs-GO-Pc, allows us to evaluate the time during which the nanocomposites described in supplementary information **Fig. S3** remain dispersed in aqueous solution. This is essential for bioapplications as it provides better stability, biocompatibility, and bioactivity to the nanocomposites [21,47]. This study was conducted at 1, 2, 3, 6, 9, 12, and 24 h. Additionally,

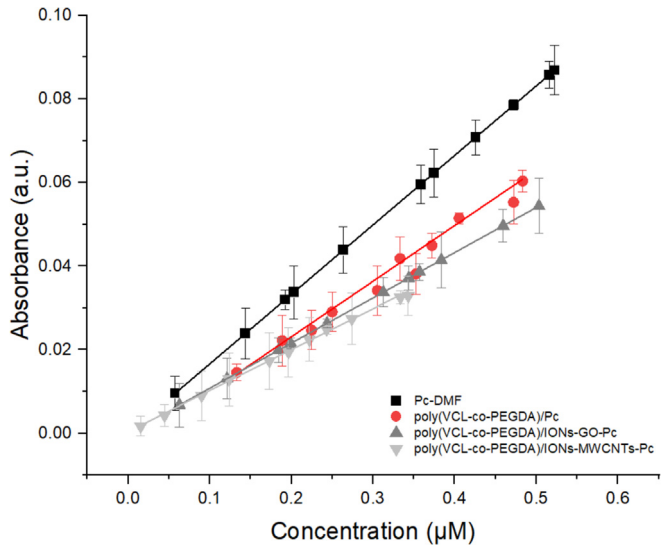


**Fig. 3.** Calibration curve of compounds based on the concentration variation of Pc.

**Table 2**
Percentage of Pc absorbance in each nanocomposite.

| Nanocomposite | Absorbance |
|---|---|
| Pc-DMF | 100% |
| poly(VCL-co-PEGDA)/Pc | 72.23% |
| poly(VCL-co-PEGDA)/IONs-MWCNTs-Pc | 62.05% |
| poly(VCL-co-PEGDA)/IONs-GO-Pc | 64.9% |

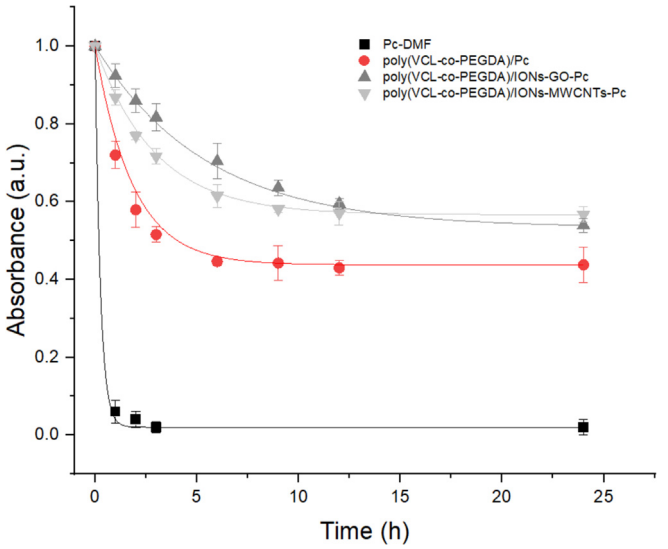


**Fig. 4. Decay curves of:** Pc-DMF, poly(VCL-co-PEGDA)/Pc, poly(VCL-co-PEGDA)/IONs-MWCNTs-Pc and poly(VCL-co-PEGDA)/IONs-GO-Pc. Pc = 8.1 μM.

it can be observed in **Fig. S3** that as time progresses, the absorbance of the B band (354 nm) increases, while the Q band (684 nm) decreases due to photooxidation of the PS without showing aggregation in 24 h.

The curves showing the stability of the nanocomposites over time are displayed in Fig. 4 and indicate that the absorbance of PS decreases exponentially. The nanocomposites were evaluated over 24 h, and it was found that the nanocomposites poly(VCL-co-PEGDA)/IONs-MWCNTs-Pc and poly(VCL-co-PEGDA)/IONs-GO-Pc reduce the release rate of PS. Table 3 shows the percentage of absorbance decrease of PS over time. It can be observed that Pc dispersed in DMF does not have controlled release since its absorbance decreases rapidly to 6% after 1 h, while in the other composites, considerable variations are observed at 24 h. The nanocomposites based on MWCNTs and GO and dispersed in the hydrogel only allowed a release of PS of 57.0% and 46.1%, respectively, whereas the Pc dispersed only in hydrogel shows a release of 43.4%, thus the process of release and dispersion of PS in the nanocomposites poly(VCL-co-PEGDA)/IONs-MWCNTs-Pc and poly(VCL-co-PEGDA)/IONs-GO-Pc can be considered very successful.

### 3.3. Photodynamic studies

To evaluate the efficiency of $^1O_2$ production in the nanocomposites: poly(VCL-co-PEGDA)/IONs-MWCNTs, poly(VCL-co-PEGDA)/IONs-GO, sample 1, and sample 2, using 630 nm light, a photobleaching assay of the oxidizable substrate DPBF was carried out in the presence of each nanocomposite. In Fig. 5, the UV–VIS spectra of each nanocomposite are presented, where a decrease in absorbance at 418 nm can be observed, corresponding to the DPBF band. This decrease in absorbance occurs as the irradiation time of DPBF + Nanocomposite increases. For the nanocomposites poly(VCL-co-PEGDA)/IONs-MWCNTs (Fig. 5a) and poly(VCL-co-

**Table 3**
Release of PS in the nanocomposites over 24 h.

| Time (h) | Pc-DMF | | poly(VCL-co-PEGDA)-Pc | | poly(VCL-co-PEGDA)/IONs-MWCNTs-Pc | | poly(VCL-co-PEGDA)/IONs-GO-Pc | |
|---|---|---|---|---|---|---|---|---|
| | **Absorbance** | **Pc Released** | **Absorbance** | **Pc Released** | **Absorbance** | **Pc Released** | **Absorbance** | **Pc Released** |
| 0 | 100% | – | 100% | – | 100% | – | 100% | – |
| 1 | 6% | 94% | 86.8 | 13.4% | 72% | 28% | 92.4% | 7.6% |
| 2 | 4% | 96% | 77% | 23% | 57.9% | 44.1% | 86% | 14% |
| 3 | 2% | 98% | 71.6% | 28.4% | 51.5% | 48.5% | 81.6% | 18.4% |
| 6 | 2% | 98% | 61.5% | 38.5% | 44.6% | 55.4% | 70.4% | 29.6% |
| 9 | 2% | 98% | 58.1% | 41.9% | 44.2% | 55.8% | 63.6% | 36.4% |
| 12 | 2% | 98% | 57% | 43% | 43% | 57% | 59.5% | 40.5% |
| 24 | 2% | 98% | 56.6% | 43.4% | 43% | 57% | 53.9% | 46.1% |

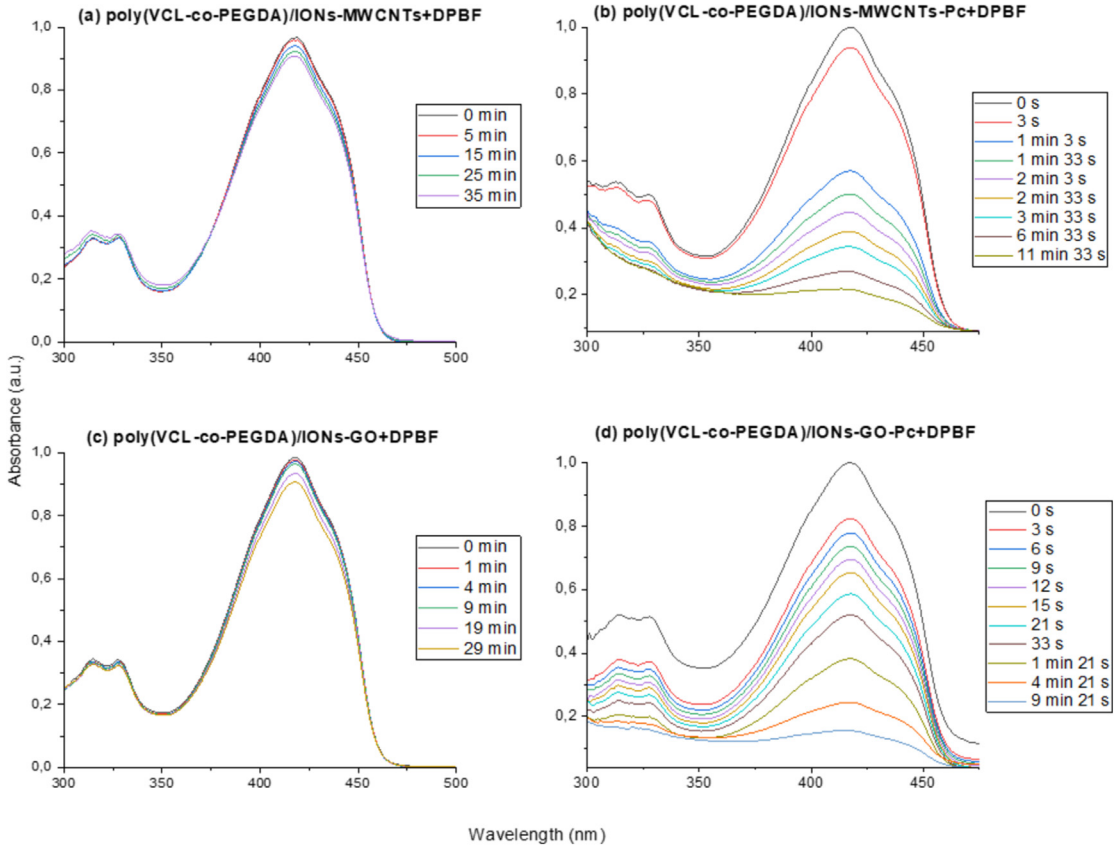


**Fig. 5. UV–Vis spectra for photodynamic analysis:** (a) poly(VCL-co-PEGDA)/IONs-MWCNTs, (b) poly(VCL-co-PEGDA)/IONs-MWCNTs-Pc, (c) poly(VCL-co-PEGDA)/IONs-GO and (d) poly(VCL-co-PEGDA)/IONs-GO-Pc. DPBF = 18.5 mM, GO = 3.47 $\mu g \cdot mL^{-1}$, MWCNTs = 3.47 $\mu g \cdot mL^{-1}$ IONs = 93.3 $\mu g \cdot mL^{-1}$, and Pc = 8.1 μM.

PEGDA)/IONs-GO (Fig. 5c**),** a slight decrease in absorbance at the 418 nm band is observed at irradiation times of 29 and 35 min, respectively. In contrast, for nanocomposites containing PS (sample 1, Fig. 5b and sample 2, Fig. 5d), a rapid decrease in absorbance at the band located at 418 nm is observed, reaching an absorbance of ~ 0, indicating that the DPBF was completely photobleaching in samples 1 and 2 after ~ 9 and 11 min of irradiation, respectively.

For each nanocomposite, absorbance curves versus irradiation time were constructed. Based on the absorbance band of DPBF located at 418 nm, an exponential decay fit was performed to obtain the photobleaching time presented in Fig. 6 shows that the nanocomposites without PS, poly(VCL-co-PEGDA)/IONs-MWCNTs and poly(VCL-co-PEGDA)/IONs-GO, have longer DPBF photobleaching times compared to those that contain PS. The photobleaching time of DPBF in nanocomposites containing GO was shorter than in those containing MWCNTs, indicating that GO has a better capacity to generate $^1O_2$ for the photobleaching of DBPF (Table 4) [48].

The presence of PS in the nanocomposites results in rapid photobleaching of DPBF. Therefore, the results indicate that the photobleaching of DPBF was mainly due to the PDT effects mediated by nanocomposites containing PS, such as poly(VCL-co-PEGDA)/IONs-MWCNTs-Pc and poly(VCL-co-PEGDA)/IONs-GO-Pc, where the nanocomposite based on GO exhibits more significant generation of $^1O_2$ than that based on MWCNTs.

### *3.4. Photothermal studies*

The photothermal study curves, shown in Fig. 7b, demonstrate that IONs, GO, and MWCNTs act as photothermal materials when irradiated with red light (630 nm) for about 100 min. These nanomaterials can reach temperatures between 50.8 and 54.8°C, mak-

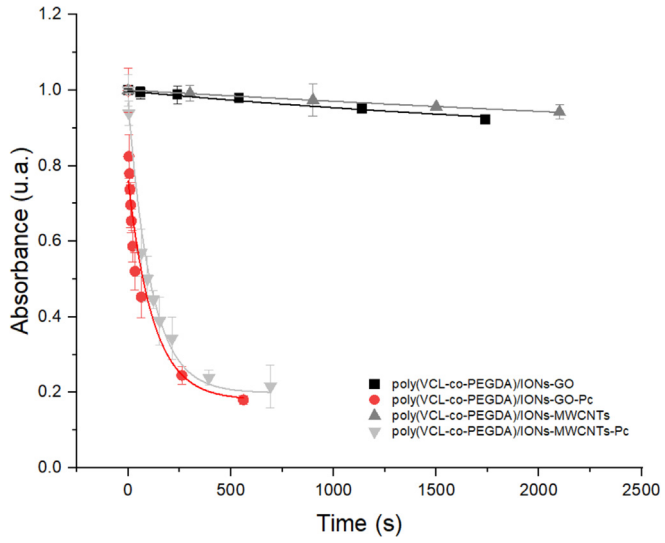


**Fig. 6. Photobleaching curves of DPBF in:** poly(VCL-co-PEGDA)/IONs-GO, poly(VCL-co-PEGDA)/IONs-GO-Pc, poly(VCL-co-PEGDA)/IONs-MWCNTs and poly(VCL-co-PEGDA)/IONs-MWCNTs-Pc. DPBF = 18.5 mM, GO = 3.47 μg·mL$^{-1}$, MWCNTs = 3.47 μg·mL$^{-1}$, IONs = 93.3 μg·mL$^{-1}$, and Pc = 8.1 μM.

**Table 4**
DPBF photobleaching time.

| Nanocomposite | DPBF photobleaching time |
|---|---|
| poly(VCL-co-PEGDA)/IONs-GO | 2866.67 ± 36.55 s = 47.78 ± 0.61 h |
| poly(VCL-co-PEGDA)/IONs-GO-Pc | 120.78 ± 0 s = 2.01 ± 0 min |
| poly(VCL-co-PEGDA)/IONs-MWCNTs | 8176.54 ± 399.19 s = 2.27 ± 0.11 h |
| poly(VCL-co-PEGDA)/IONs-MWCNTs-Pc | 152.26 ± 9.04 s = 1.87 ± 0.15 min |

ing them suitable for use in Photothermal Therapy (PTT), due to their ability to convert red and near-infrared (NIR) light into heat, and to carry drugs, as mentioned in the literature [49,50]. In the photothermal study curves of Fig. 7c, it can also be observed that the nanocomposites poly(VCL-co-PEGDA), poly(VCL-co-PEGDA)/IONs-MWCNTs-Pc, and poly(VCL-co-PEGDA)/IONs-GO-Pc irradiated with red light (630 nm) for about 100 min show a slight decrease in temperature compared to the thermal curve of deionized water (control, Fig. 7a), and around 80 min of irradiation, the curves of the nanocomposites dispersed in hydrogel reach temperatures close to that of deionized water.

The curves of the IONs, GO, and MWCNTs nanocomposites raised their temperature about 10°C higher relative to the control sample (deionized water) and the nanocomposites poly(VCL-co-PEGDA)/IONs-MWCNTs-Pc and poly(VCL-co-PEGDA)/IONs-GO-Pc. It can be concluded that the poly(VCL-co-PEGDA) hydrogel can absorb a significant amount of energy without increasing its temperature. This is expected because its main components, VCL and PEGDA, have good heat capacities [51,52], therefore, the hydrogel would inherit this property. This feature explains why the nanocomposites dispersed in hydrogel maintain a temperature similar to the temperature of the control sample (deionized water) when irradiated for more than 100 min with red light (630 nm), that is, there is no photothermal effect in the magnetic nanocomposites dispersed in hydrogel. Around 30 to 45 min, all nanocomposites reach a threshold temperature that does not change when irradiated for longer periods.

### 3.5. Magnetic studies

The magnetic properties of three samples—sample 1, sample 2, and Iron Oxide Nanoparticles (IONs) were analyzed to determine how dispersion within a hydrogel matrix affects the magnetization of these nanocomposites.

Each sample displayed characteristic ferromagnetic (FM) behavior typical of IONs, with minimal coercivity (<2 mT at room temperature and <5 mT at −210°C). This low coercivity indicates that the IONs are not directly bonded to the carbon structures, as direct bonding usually results in much higher coercivities (hundreds of mT). This observation is consistent with the weak hydrogen bonds between the IONs and carbon structures identified in the FT-IR spectroscopy results.

The magnetization versus field (M vs. H) curves for the samples at −210°C and +20°C are presented in Figs. 8a,b,c. The saturation magnetization ($M_S$) as a function of temperature was derived using the standard law of approach to saturation (LAS) [27,53,54], which incorporates non-ferromagnetic contributions such as those from disordered layers of nanoparticles. The fitting of the magnetization curves (M(H)) for applied fields from 1 to 3 Tesla is shown in Figs. 8a,b,c.

The saturation magnetization ($M_S$) values, adjusted for the mass fraction of nanoparticles, were calculated across a temperature range from −210°C to +60°C (Figs. 8d,e,f). Samples 1 and 2 exhibited significantly lower magnetization values due to the high hydrogel content (>98% of the mass). The adjusted saturation magnetization values account for 1.45% and 1.41% nanoparticle mass fractions for sample 1 and sample 2, respectively.

The temperature dependence of $M_S$ for all samples follows Bloch's law, indicating that $M_S$ decreases with increasing temperature due to the thermal excitation of spin waves. The spin wave constant ($B$) values for the samples were found to be within the typical range for IONs systems, indicating similar thermally induced magnetic field excitations [55–57].

By comparing the saturation magnetization at absolute zero ($M_0$) with that of pure iron ($M_{Fe}$ = 222 emu·g$^{-1}$), the ferromagnetic

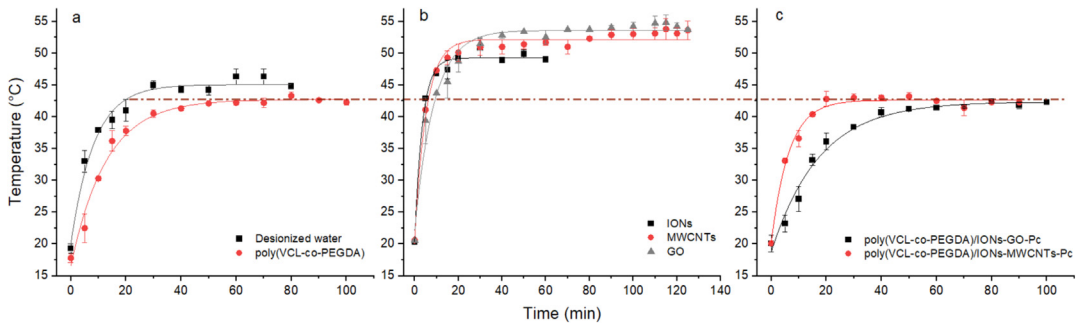


**Fig. 7. Thermal studies:** (a) deionized water (control), poly(VCL-co-PEGDA), (b) IONs, GO, MWCNTs, (c) poly(VCL-co-PEGDA)/IONs-MWCNTs-Pc and poly(VCL-co-PEGDA)/IONs-GO-Pc. GO = 3.47 μg·mL$^{-1}$, MWCNTs = 3.47 μg·mL$^{-1}$, IONs = 93.3 μg·mL$^{-1}$, and Pc = 8.1 μM.

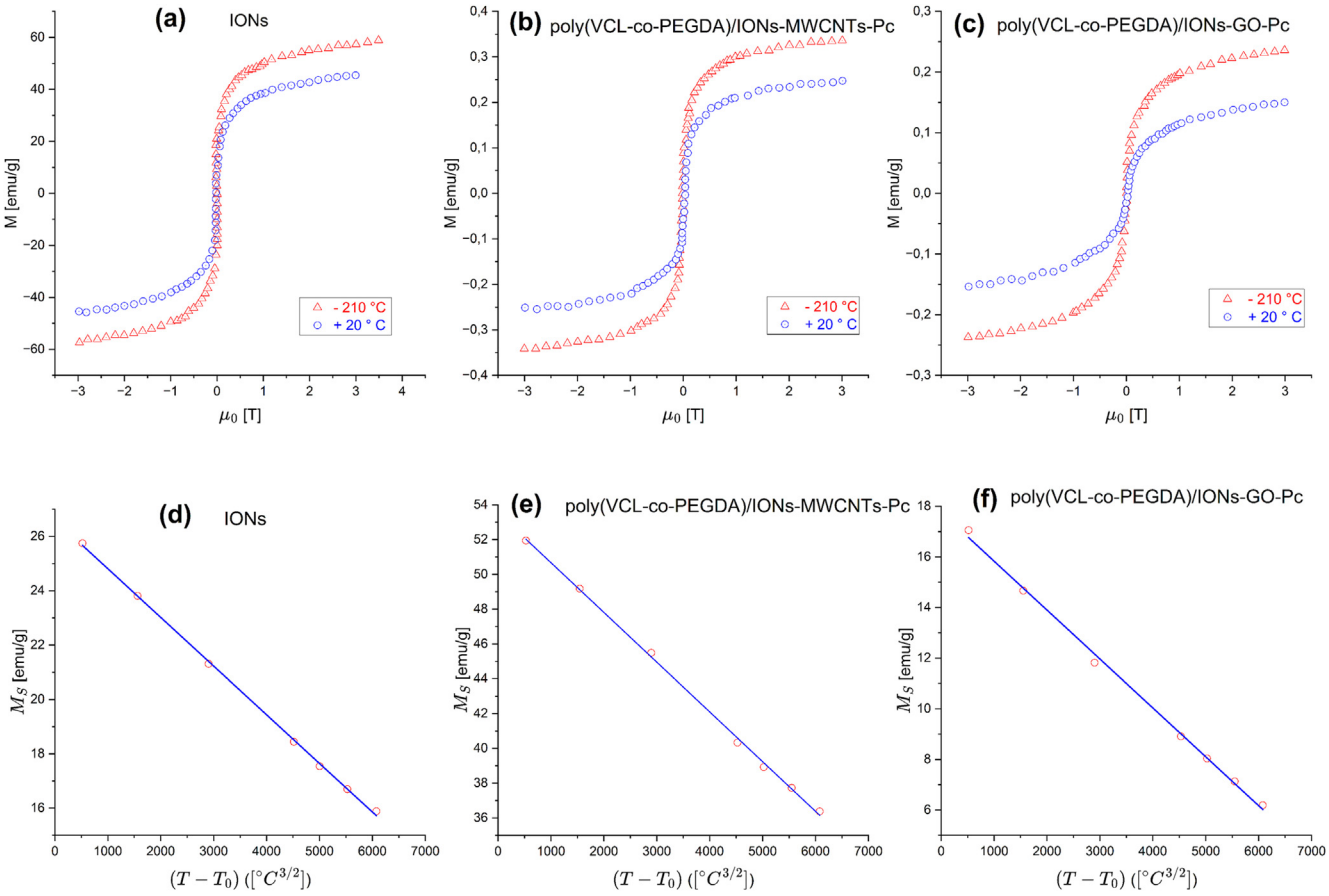


**Fig. 8. Magnetization vs. applied magnetic field:** (a)IONs, (b) sample 1, and (c) sample 2. Saturation magnetization as a function of temperature: (d) IONs, (e) sample 1 and (f) sample 2.

**Table 5**
Magnetic parameters.

| Sample | $B$ ($°C^{-3/2}$) | $M_0$ ($emu \cdot g^{-1}$) | $M_s$ ($emu \cdot g^{-1}$) | $f$ (%) |
|---|---|---|---|---|
| **IONs** | $4.5 \times 10^{-5}$ | 52.1 | 40.1 | 23.5 |
| **Sample 1** | $5.8 \times 10^{-5}$ | 25.5 | 17.9 | 11.5 |
| **Sample 2** | $8.3 \times 10^{-5}$ | 15.9 | 9.3 | 7.2 |

volume fraction ($f\% = \frac{M_0}{M_{Fe}}$,) was estimated. The values indicate a lower ferromagnetic volume fraction in samples 1 and 2 compared to IONs alone, suggesting the formation of a magnetically inactive layer due to the hydrogel matrix. These values are shown in Table 5.

The dispersion of IONs within the hydrogel matrix significantly affects the magnetic properties of the nanocomposites. The weak hydrogen bonds between IONs and carbon structures lead to minimal coercivity, and the high hydrogel content results in lower overall magnetization values. The hydrogel appears to form a magnetically inactive layer, reducing the effective magnetic moment of the samples [55–57].

### 3.6. Morphological studies of magnetic nanocomposites

The functionalized nanocomposites poly(VCL-co-PEGDA)/IONs-MWCNTs-Pc and poly(VCL-co-PEGDA)/IONs-GO-Pc were characterized by SEM, TEM, EDS, and XRD techniques. The results of these characterizations for the nanocomposites (GO, MWCNTS, IONs, IONs-GO, IONs-MWCNTs, poly(VCL-co-PEGDA)/IONs-MWCNTs, poly(VCL-co-PEGDA)/IONs-GO, poly(VCL-co-PEGDA)/IONs-MWCNTs-Pc and poly(VCL-co-PEGDA)/IONs-GO-Pc are presented in supplementary information (**Fig. S4**, **Fig. S5**, **Fig. S6**, **Fig. S7**, **Fig. S8**. **Fig. S9**, **Fig. S10**, **Fig. S11**, **and Fig. S12**.

The SEM and TEM images in Fig. 9 and Fig. 10 show the morphology of IONs with a spherical shape and an average size of ~ 73.8 nm can be observed in Figs. 9a,c and Fig. 10a. In Fig. 9b MWCNTs, which are fibrous in shape and in the TEM image (Fig. 10b), the internal structure and walls of the MWCNTs can be observed. In Fig. 9c and Fig. 10c, the structure of large GO sheets is observed. **Fig. S4d** presents the height profile of GO and indicates that the thickness of the GO is approximately 2.82 nm, which suggests that the sheet is four layers thick. Various sizes of GO sheets are represented, but the most common is approximately 2.15 µm. Figs. 9d,e and Figs. 10d,e**,** show the morphology of the hydrogel coating on IONs-MWCNTs-Pc and IONs-GO-Pc and due to the presence of the coating, it is difficult to differentiate the structures covered by the hydrogel.

In Fig. 10f, the XRD pattern for the IONs-GO sample is presented, showing the diffraction peaks of the IONs decorating the

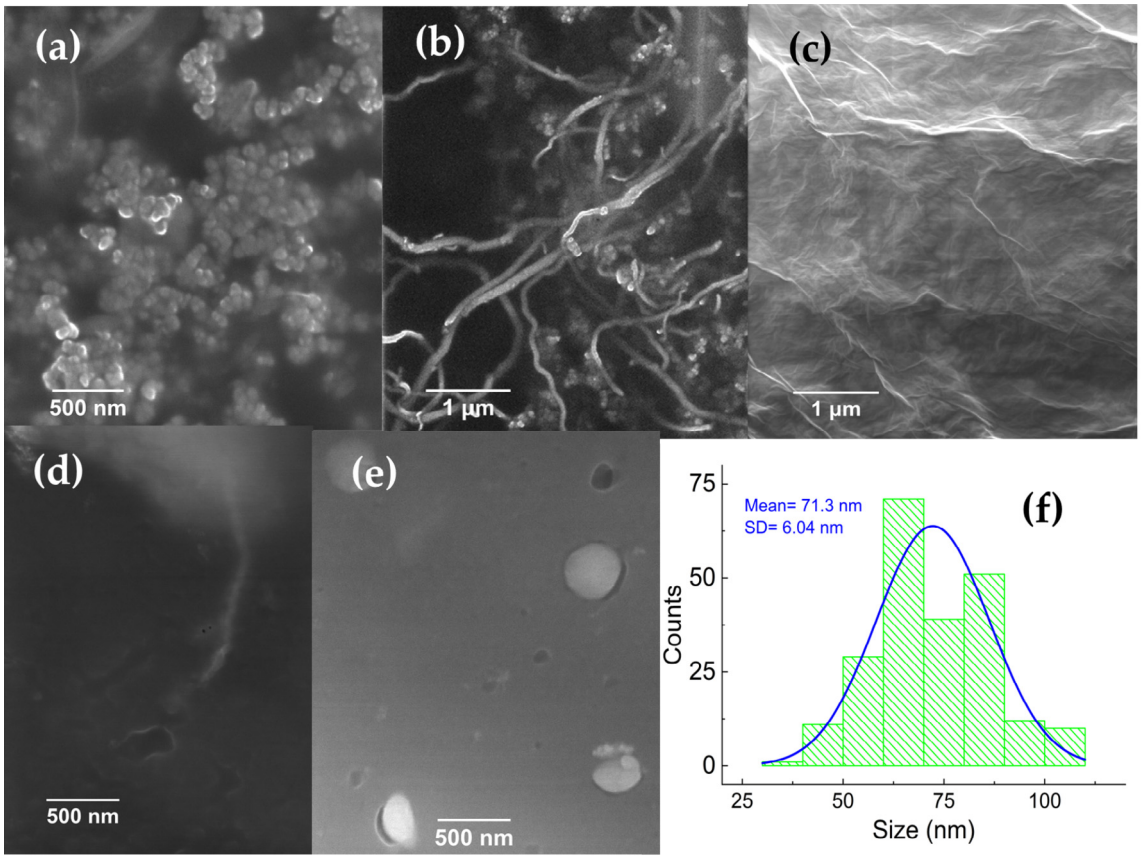


**Fig. 9.** SEM images of (a) IONS, (b) purified MWCNTs, (c) GO, (d) poly(VCL-co-PEGDA)/IONs-MWCNTs-Pc, (e) TEM of poly(VCL-co-PEGDA)/IONs-GO-Pc, (f) IONs size distribution.

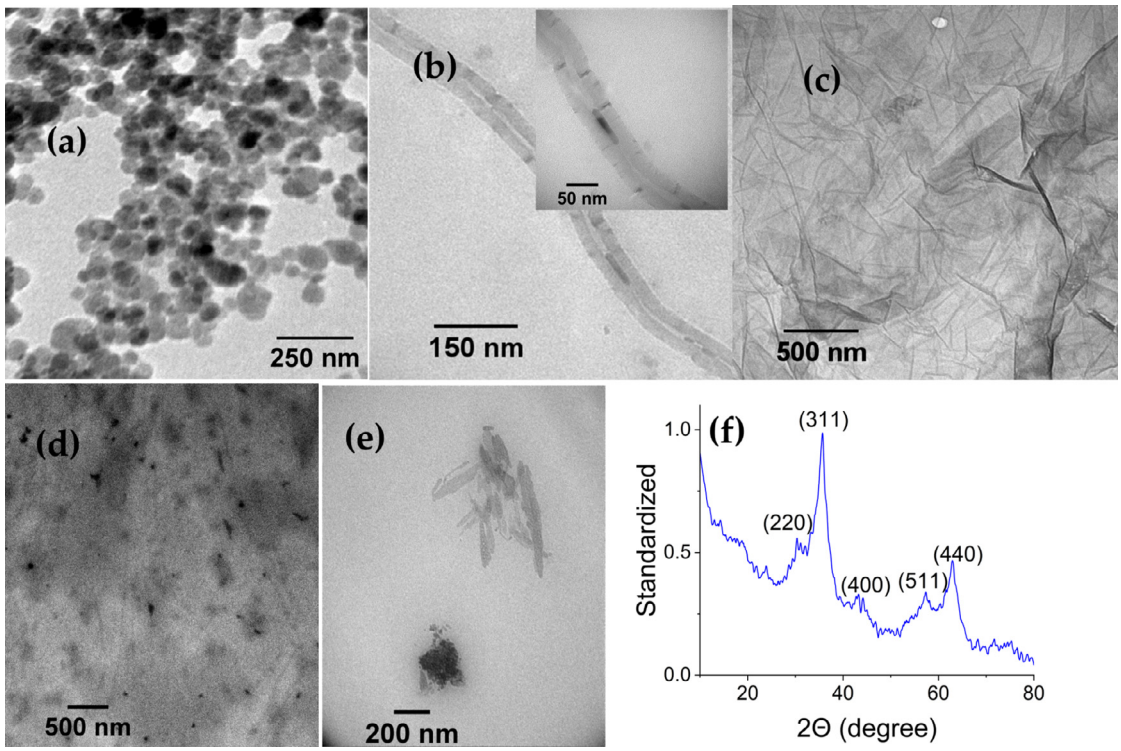


**Fig. 10.** TEM images of (a) IONs, (b) MWCNTs, (c) GO, (d) poly(VCL-co-PEGDA)/IONs-MWCNTs-Pc, (e) TEM of poly(VCL-co-PEGDA)/IONs-GO-Pc, and (f) DRX of IONs-GO.

GO at 2θ = 30.2°, 35.54°, 43°, 54°, 57°, and 63°. These peaks indicate that the IONs retain their original crystalline structure after functionalization, consistent with the literature [58,59].

### 3.7. Antimicrobial effect evaluation

The antimicrobial effect of the magnetic nanocomposites: poly (VCL-co-PEGDA)/IONs-MWCNTs-Pc (sample 1, S1) and poly(VCL-co-PEGDA)/IONs-GO-Pc (sample 2, S2) was evaluated based on the PDT strategy. These nanocomposites were dispersed among the microorganisms *S. aureus, E. coli,* and irradiated with red light at 630 nm.

The bactericidal efficacy of the magnetic nanocomposites poly (VCL-co-PEGDA)/IONs-MWCNTs-Pc (sample 1, S1) and poly(VCL-co-PEGDA)/IONs-GO-Pc (sample 2, S2) was assessed using the PDT approach. These nanocomposites were mixed with the microorganisms *S. aureus 1*, *S. aureus 2* and *E. coli* and exposed to 630 nm red light. The outcomes for each bacterial colony are depicted in Fig. 11. The histograms display a standardized LOG (CFU $mL^{-1}$) scale set to 1. Concentrations of $10^7$ CFU·$mL^{-1}$ for *S. aureus 1* and *2*, $10^6$ CFU·$mL^{-1}$ for *E. coli*, were employed. The colony count data post-irradiation with a red LED (630 nm) shows that for *S. aureus 1*, *S. aureus 2 E. coli* (Figs. 11a,b,c), the counts in the S1+ light and S2+ light samples were significantly reduced compared to the control group (***$p \leq 0.001$). The number of colonies for these three microbes in the + darkness samples did not differ from the control, yet in the S1 + light and S2 + light samples, the counts were significantly lower than the control group (***$p \leq 0.001$). This implies that following the irradiation, the S1 and S2 nanocomposites can effectively reduce the populations of *E. coli*, *S. aureus 1*, and some colonies of *S. aureus 2*.

### 3.8. Discussion

According to the results obtained, the nanocomposites poly (VCL-co-PEGDA)/IONs-MWCNTs-Pc and poly(VCL-co-PEGDA)/IONs-GO-Pc exhibit ferromagnetic character, typical of nanocomposites containing IONs. Moreover, they exhibit low saturation magnetization due to being coated with a diamagnetic hydrogel layer, which is consistent with studies conducted by Mahdavi et al. [60], Donadel et al. [61] and Qu et al. [62]. The IONs are used in various bioapplications, and the IONs synthesized and functionalized in this study showed that surface modification leads to a reduction in saturation magnetization, with values ranging from 67 to 22 emu·$g^{-1}$. According to the literature, as IONs are embedded in a non-magnetic polymeric matrix, the magnetization values decrease, but do not change the magnetic nature of the IONs [60,62].

In the study of the physical and magnetic properties of these nanocomposites, it was demonstrated that they have the ability to prevent the early quenching of the fluorescence of the PS. Therefore, it can be said that the synthesized nanocomposites enhance the photodynamic effect. This is consistent with the information provided in the works of Huang et al. [63] and Xiao et al. [64]. Additionally, it was demonstrated that the poly(VCL-co-PEGDA) hydrogel is capable of keeping the magnetic nanocomposites containing

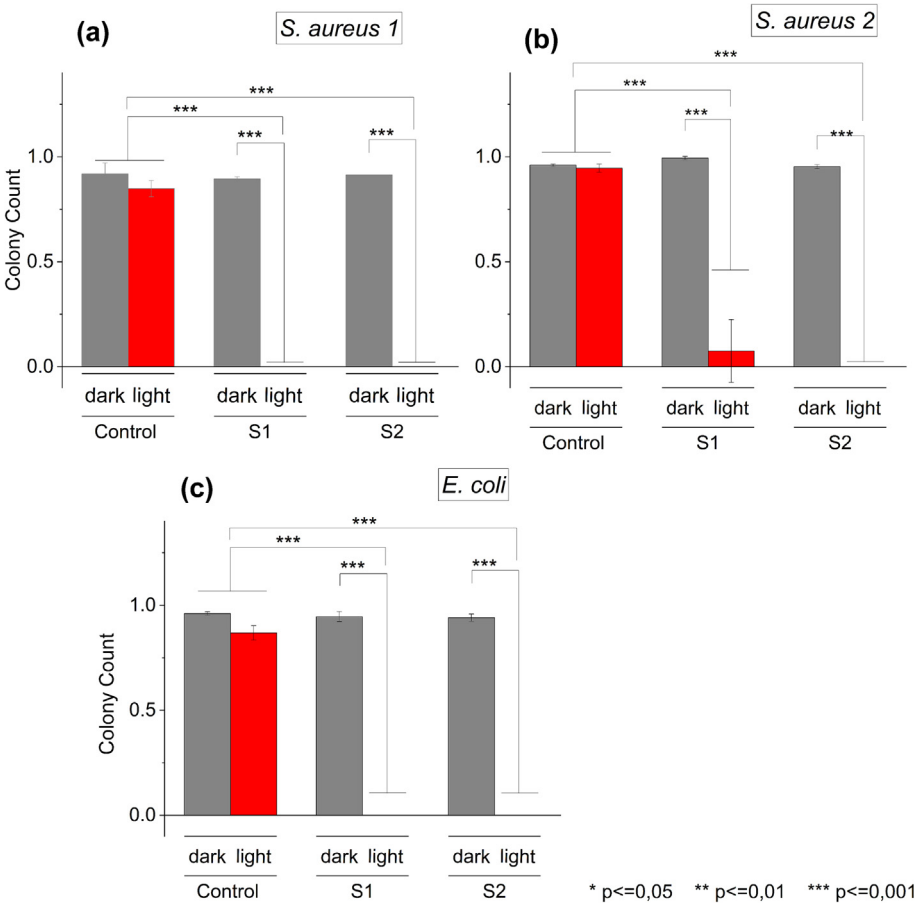


**Fig. 11. Antimicrobial effect based on PDT.** Standardized results of LOG(CFU·$mL^{-1}$) for (a) *S. aureus* 1; (b) *S. aureus* 2; and (c) *E. coli*, utilizing nanocomposites S1 and S2. GO = 3.47 μg·$mL^{-1}$, MWCNTs = 3.47 μg·$mL^{-1}$, IONs = 93.3 μg·$mL^{-1}$, and Pc = 8.1 μM. The irradiation time was 30 min. Significant differences in means were found according to Tukey's test (***$p \leq 0.001$).

the hydrophobic PS dispersed over 24 h. This is due to the hydrogel having a hydrophobic core capable of interacting with hydrophobic compounds and a hydrophilic surface that allows it to be water-soluble as mentioned by Romero et al. [25]. It also demonstrates the hydrogel's capability to be used as a drug delivery system, being able to release 57% of the drug from sample 1 and 46.1% from sample 2 over 24 h at a temperature of 38°C [25].

The antimicrobial studies showed in the quantitative result of colony counts of the three types of microorganisms that all the nanocomposites are capable of eliminating some of the microorganisms used in this study after irradiation with red light of 635 nm. This is consistent with the studies on antimicrobial nanomaterials based on PDT presented by Ren et al. [65], Huo et al. [66], and Liu et al. [67]. Moreover, it was demonstrated that the nanocomposite poly(VCL-co-PEGDA)/IONs-MWCNTs-Pc (S2) is the best due to its capacity to completely eliminate the three types of microorganisms, while the nanocomposite poly(VCL-co-PEGDA)/IONs-GO-Pc (S1) completely eliminated only the colonies of *E. coli* and *S. aureus 1* and partially eliminated *S. aureus 2*.

For the samples with hydrogel and photosensitizer (S1 + light and S2 + light), from Fig. 11, it can be deduced that the elimination of the microorganisms *S. aureus 1, S. aureus 2* and *E. coli* occurred due to the photodynamic effect, as supported by the research of Mei et al. [68], and data reported by Xu et al. [69]. This is also supported by the results of the photodynamic study that shows the ability of the nanocomposites to generate a significant amount of $^1O_2$ due to the photodynamic effect of the carbon-based materials and to a greater extent by the PS [69].

It was deduced that there is no elimination by photothermal effect because Fig. 7c demonstrates that the hydrogel is capable of maintaining the system at temperatures around 43.3°C while it is irradiated with red light (630 nm). The temperature curves of the nanocomposites dispersed in hydrogel reach a maximum of 43.3°C over a duration of 100 min of irradiation, which represents a lower temperature compared to the nanocomposites dispersed in water that reach approximately 54°C after 100 min of irradiation with red light (630 nm). The increase in temperature of the nanocomposites without hydrogel is attributed to the inherent photothermal effect of nanoparticles and carbon-based materials. Consequently, S1 and S2 could potentially be applied in human subjects in the future, given that hydrogel is biocompatible and the body can withstand temperatures up to 43°C during the therapy period [70,71].

The control samples irradiated with red light showed no microbial elimination through thermal increase, since the involved in this study can withstand high temperatures around 60°C [28,72]. Thus, microbial eradication is achieved through the photodynamic actions observed in samples S1 and S2. The incorporation of these nanocomposites into the *microorganisms* is facilitated by the direct interaction between the microorganism and nanocomposite, and the PDT effects seen in S1 and S2. Several scholars, including Lagos et al. [73] and Patil et al. [24], have analyzed these effects, noting that PS, GO, and MWCNTs can target multiple organelles. The photodynamic activity of nanocomposites S1 and S2 leads to the production of reactive oxygen species (ROS), causing physical membrane damage and oxidative [24,73,74]. This oxidative stress, triggered by PDT, alters calcium and lipid metabolism, producing cytokines and mediators that trigger apoptosis through mitochondrial pathways and protein oxidation [24,73–76]. This process is determined to be responsible for the death of the microorganisms *S. aureus 1, S. aureus 2* and *E. coli* in the study. Furthermore, research by Dias et al. [77], and Liu et al. [78], has investigated how these carbon-based nanocomposites and IONs are excreted through the biliary and urinary systems.

## 4. Conclusions

In this study, the nanocomposites poly(VCL-co-PEGDA)/IONs-MWCNTs-Pc and poly(VCL-co-PEGDA)/IONs-GO-Pc were synthesized to eliminate three types of microbial colonies: *S. aureus 1, S. aureus 2* and *E. coli,* using the PDT strategy.

The nanocomposites were characterized through spectroscopies such as FT-IR, Raman, and UV–VIS; microscopies such as SEM and TEM; and other techniques including EDS, VSM, and XRD. These methods allowed for the determination of the physical and chemical characteristics of the nanocomposites. This analysis showed the functionalization of Pc in the IONs-GO and IONs-MWCNTs nanocomposites in the presence of the poly(VCL-co-PEGDA) hydrogel. Furthermore, the presence of IONs anchored to the GO and MWCNT structures was determined, which provides magnetic properties to the nanocomposites. Although the magnetization values obtained from the nanocomposites dispersed in hydrogel are small, they fall within the favorable range used for biomedical applications, typically between 8 and 100 $emu \cdot g^{-1}$. Therefore, the nanocomposites developed in this study are suitable for biomedical applications that utilize external magnetic fields.

The optical (absorbance spectra), magnetic, and morphological characterizations indicated that the nanocomposites: IONs-GO-Pc and IONs-MWCNTs-Pc, are dispersed in the poly(VCL-co-PEGDA) hydrogel. The dispersion of the nanocomposites is critical in PDT to ensure a uniform distribution within the target tissue or cell, which directly influences the efficiency and efficacy of the therapy. Uniform dispersion enables maximum light absorption and efficient energy transfer processes. Moreover, it facilitates maximum interaction between the elements of the nanocomposites, such as the PS, IONs-GO, and IONs-MWCNTs, with the target, thereby improving the therapeutic outcome and minimizing damage to the surrounding healthy tissues. Additionally, the optical properties of the nanocomposites demonstrate that due to their broad light absorption spectrum, rapid photodegradation of the Pc is prevented, which is essential in PDT techniques. In summary, these characteristics are fundamental for achieving uniform distribution, maximizing interaction with the target, optimizing optical properties, ensuring stability, and achieving reproducibility in PDT-based applications.

Through photodynamic analysis of the two nanocomposites applicable in PDT: poly(VCL-co-PEGDA)/IONs-MWCNTs-Pc and poly(VCL-co-PEGDA)/IONs-GO-Pc, irradiated with low-dose red light, it was determined that the nanocomposite poly(VCL-co-PEGDA)/IONs-GO-Pc shows higher photodynamic efficiency than the MWCNTs-based nanocomposite. This is due to its faster photobleaching of DPBF. The rapid photobleaching of DPBF caused by the nanocomposite containing GO and Pc was due to GO's ability to transport a significant amount of Pc and IONs, thanks to its large specific area. Additionally, GO contributed to the PS in generating $^1O_2$, a key feature for PDT, and since the nanocomposites are dispersed in a hydrogel, they are suitable for controlled release systems of PS, with promising applications for PDT.

In the end, it was shown that the nanocomposites poly(VCL-co-PEGDA)/IONs-GO-Pc and poly(VCL-co-PEGDA)/IONs-MWCNTs-Pc are effective in eradicating colonies of *S. aureus 1, S. aureus 2* and *E. coli,* thereby qualifying them as broad-spectrum antimicrobial agents in photodynamic therapy (PDT).

## CRediT authorship contribution statement

**Coralia Cuadrado:** Writing – review & editing, Writing – original draft, Visualization, Validation, Supervision, Project administration, Methodology, Investigation, Funding acquisition. **Alex**

**Mantilla:** Writing – review & editing, Writing – original draft, Visualization, Validation, Software, Investigation, Funding acquisition, Data curation. **Luis Hidalgo:** Writing – review & editing, Validation, Resources, Methodology, Investigation, Funding acquisition. **Diego Punina:** Writing – review & editing, Visualization, Validation, Investigation, Data curation.

## Financial support

This research received no external funding.

## Declaration of competing interest

The authors declare no conflict of interest.

## Acknowledgments

Escuela Superior Politécnica de Chimborazo.

## Supplementary material

https://doi.org/10.1016/j.ejbt.2024.08.002.

## Data availability

Data will be made available on request.

## References

[1] World Health Organization. Managing epidemics: Key facts about major deadly diseases. 1st ed. Vol. 1, World Health Organization. Luxembourg: World Health Organization; 2018.
[2] Makabenta JMV, Nabawy A, Li C-H, et al. Nanomaterial-based therapeutics for antibiotic-resistant bacterial infections. Nat Rev Microbiol 2021;19(1):23–36. https://doi.org/10.1038/s41579-020-0420-1. PMid: 32814862.
[3] Dadgostar P. Antimicrobial resistance: Implications and costs. Infect Drug Resist 2019;12:3903–10. https://doi.org/10.2147/IDR.S234610. PMid: 31908502.
[4] World Health Organization. Antimicrobial resistance. 2023 [cited 2023 Apr 6]. Available from: https://www.who.int/news-room/fact-sheets/detail/antimicrobial-resistance.
[5] Ali A, Ovais M, Cui X, et al. Safety assessment of nanomaterials for antimicrobial applications. Chem Res Toxicol 2020;33(5):1082–109. https://doi.org/10.1021/acs.chemrestox.9b00519. PMid: 32302095.
[6] Zhao Y, Zhang Z, Pan Z, et al. Advanced bioactive nanomaterials for biomedical applications. Exploration 2021;1(3):. https://doi.org/10.1002/EXP.20210089 20210089.
[7] Zhu H, Cheng P, Chen P, et al. Recent progress in the development of near-infrared organic photothermal and photodynamic nanotherapeutics. Biomater Sci 2018;6(4):746–65. https://doi.org/10.1039/C7BM01210A. PMid:29485662.
[8] Wang Y, Wei T, Qu Y, et al. Smart, photothermally activated, antibacterial surfaces with thermally triggered bacteria-releasing properties. ACS Appl Mater Interfaces 2020;12(19):21283–91. https://doi.org/10.1021/acsami.9b17581. PMid:31709795.
[9] de Menezes BRC, Rodrigues KF, da Silva Fonseca BC, et al. Recent advances in the use of carbon nanotubes as smart biomaterials. J Mater Chem B 2019;7(9):1343–60. https://doi.org/10.1039/C8TB02419G. PMid: 32255006.
[10] Wang C, Makvandi P, Zare EN, et al. Advances in antimicrobial organic and inorganic nanocompounds in biomedicine. Adv Ther 2020;3(8):. https://doi.org/10.1002/adtp.202000024 2000024.
[11] Al-Jumaili A, Alancherry S, Bazaka K, et al. Review on the antimicrobial properties of carbon nanostructures. Materials 2017;10(9):1066. https://doi.org/10.3390/ma10091066.
[12] Klausen M, Ucuncu M, Bradley M. Design of photosensitizing agents for targeted antimicrobial photodynamic therapy. Molecules 2020;25(22):5239. https://doi.org/10.3390/molecules25225239. PMid: 33182751.
[13] Anju VT, Paramanantham P, Sb SL, et al. Antimicrobial photodynamic activity of rose bengal conjugated multi walled carbon nanotubes against planktonic cells and biofilm of *Escherichia coli*. Photodiagnosis Photodyn Ther 2018;24:300–10. https://doi.org/10.1016/j.pdpdt.2018.10.013. PMid: 30342101.
[14] Wu W, Wu Z, Yu T, et al. Recent progress on magnetic iron oxide nanoparticles: Synthesis, surface functional strategies and biomedical applications. Sci Technol Adv Mater 2015;16(2):. https://doi.org/10.1088/1468-6996/16/2/023501. PMid: 27877761023501.
[15] de Toledo LD, Rosseto HC, Bruschi ML. Iron oxide magnetic nanoparticles as antimicrobials for therapeutics. Pharm Dev Technol 2018;23(4):316–23. https://doi.org/10.1080/10837450.2017.1337793. PMid: 28565928.
[16] Berry CC, Curtis ASG. Functionalisation of magnetic nanoparticles for applications in biomedicine. J Phys D Appl Phys 2003;36(13):R198–206. https://doi.org/10.1088/0022-3727/36/13/203.
[17] Pankhurst QA, Connolly J, Jones SK, et al. Applications of magnetic nanoparticles in biomedicine. J Phys D Appl Phys 2003;36(13):R167–81. https://doi.org/10.1088/0022-3727/36/13/201.
[18] Colombo M, Carregal-Romero S, Casula MF, et al. Biological applications of magnetic nanoparticles. Chem Soc Rev 2012;41(11):4306–34. https://doi.org/10.1039/c2cs15337h. PMid: 22481569.
[19] Cheng L, Wang C, Feng L, et al. Functional nanomaterials for phototherapies of cancer. Chem Rev 2014;114(21):10869–939. https://doi.org/10.1021/cr400532z. PMid: 25260098.
[20] Kausar A. Nanocarbon in polymeric nanocomposite hydrogel—Design and multi-functional tendencies. Polymer-Plast Technol Mater 2020;59(14):1505–21. https://doi.org/10.1080/25740881.2020.1757106.
[21] Yi J, Choe G, Park J, Lee JY. Graphene oxide-incorporated hydrogels for biomedical applications. Polym J 2020;52(8):823–37. https://doi.org/10.1038/s41428-020-0350-9.
[22] Teradal NL, Jelinek R. Carbon nanomaterials in biological studies and biomedicine. Adv Healthc Mater 2017;6(17):. https://doi.org/10.1002/ADHM.201700574. PMid: 28777021700574.
[23] Maiti D, Tong X, Mou X, et al. Carbon-based nanomaterials for biomedical applications: A recent study. Front Pharmacol 2019;9:1401. https://doi.org/10.3389/fphar.2018.01401. PMid: 30914959.
[24] Patil TV, Patel DK, Dutta SD, et al. Carbon nanotubes-based hydrogels for bacterial eradiation and wound-healing applications. Appl Sci 2021;11(20):9550. https://doi.org/10.3390/app11209550.
[25] Romero JF, Díaz-Barrios A, González G. Biocompatible thermo-responsive N-vinylcaprolactam based hydrogels for controlled drug delivery systems. Bionatura 2021;6(2):1712–9. https://doi.org/10.21931/RB/2021.06.02.8.
[26] Soler MAG, Qu F. Raman spectroscopy of iron oxide nanoparticles. In: Kumar CSSR, editor. Raman Spectroscopy for Nanomaterials Characterization. Berlin, Heidelberg: Springer Berlin Heidelberg; 2012. https://doi.org/10.1007/978-3-642-20620-7_14.
[27] Hauser H, Jiles DC, Melikhov Y, et al. An approach to modeling the dependence of magnetization on magnetic field in the high field regime. J Magn Magn Mater 2006;300(2):273–83. https://doi.org/10.1016/j.jmmm.2005.05.017.
[28] Kaur J, Ledward DA, Park RWA, et al. Factors affecting the heat resistance of Escherichia coli O157: H7. Lett Appl Microbiol 1998;26(4):325–30. https://doi.org/10.1046/j.1472-765X.1998.00339.x. PMid: 9633099.
[29] Abrinaei F, Kimiagar S, Zolghadr S. Hydrothermal synthesis of hematite-GO nanocomposites at different GO contents and potential application in nonlinear optics. Opt Mater 2019;96:. https://doi.org/10.1016/j.optmat.2019.109285 109285.
[30] Al-Ruqeishi MS, Mohiuddin T, Al-Moqbali M, et al. Graphene oxide synthesis: Optimizing the Hummers and Marcano methods. Nanosci Nanotechnol Lett 2020;12(1):88–95. https://doi.org/10.1166/nnl.2020.3074.
[31] Santoro G, Domingo C. Espectroscopía Raman de nanotubos de carbono. Opt Pura Apl 2007;40(2):175–86.
[32] Dresselhaus M, Dresselhaus G, Saito R, et al. Raman spectroscopy of carbon nanotubes. Phys Rep 2005;409(2). https://doi.org/10.1016/j.physrep.2004.10.006.
[33] Marković Z, Jovanović S, Kleut D, et al. Comparative study on modification of single wall carbon nanotubes by sodium dodecylbenzene sulfonate and melamine sulfonate superplasticiser. Appl Surf Sci 2009;255(12):6359–66. https://doi.org/10.1016/j.apsusc.2009.02.016.
[34] Bokobza L, Zhang J. Raman spectroscopic characterization of multiwall carbon nanotubes and of composites. ExpressPolym Lett 2012;6(7):601–8. https://doi.org/10.3144/expresspolymlett.2012.63. PMid: 25435600.
[35] Cançado LG, Jorio A, Ferreira EHM, et al. Quantifying defects in graphene via Raman spectroscopy at different excitation energies. Nano Lett 2011;11(8):3190–6. https://doi.org/10.1021/nl201432g. PMid: 21696186.
[36] Hafiz SM, Ritikos R, Whitcher TJ, et al. A practical carbon dioxide gas sensor using room-temperature hydrogen plasma reduced graphene oxide. Sens Actuators B Chem 2014;193:692–700. https://doi.org/10.1016/j.snb.2013.12.017.
[37] Ramirez S, Chan K, Hernandez R, et al. Thermal and magnetic properties of nanostructured densified ferrimagnetic composites with graphene - graphite fillers. Mater Des 2017;118:75–80. https://doi.org/10.1016/j.matdes.2017.01.018.
[38] Satheesh M, Paloly AR, Krishna Sagar CK, et al. Improved coercivity of solvothermally grown hematite ($\alpha$-$Fe_2O_3$) and hematite/graphene oxide nanocomposites ($\alpha$-$Fe_2O_3$/GO) at low temperature. Phys Status Solidi A 2018;215(2):. https://doi.org/10.1002/pssa.201700705 1700705.
[39] Romero MP, Gobo NRS, de Oliveira KT, et al. Photophysical properties and photodynamic activity of a novel menthol–zinc phthalocyanine conjugate incorporated in micelles. J Photochem Photobiol A Chem 2013;253:22–9. https://doi.org/10.1016/j.jphotochem.2012.12.009.

[40] Wang Y, Song X, Shao S, et al. An efficient, soluble, and recyclable multiwalled carbon nanotubes-supported TEMPO for oxidation of alcohols. RSC Adv 2012;2 (20):7693. https://doi.org/10.1039/c2ra21206d.
[41] Bera M, Chandravati P, Gupta P, et al. Facile one-pot synthesis of graphene oxide by sonication assisted mechanochemical approach and its surface chemistry. J Nanosci Nanotechnol 2018;18(2):902–12. https://doi.org/10.1166/jnn.2018.14306. PMid: 29448514.
[42] Chen P, Marshall AS, Chi S, et al. Luminescent quadrupolar borazine oligomers: Synthesis, photophysics, and two-photon absorption properties. Chem – A Eur J 2015;21(50):18237–47. https://doi.org/10.1002/chem.201502268. PMid: 26514664.
[43] Meier H, Gerold J, Kolshorn H, et al. Extension of conjugation leading to bathochromic or hypsochromic effects in OPV series. Chemistry 2004;10 (2):360–70. https://doi.org/10.1002/chem.200305447. PMid: 14735504.
[44] Wu W, Shen J, Gai Z, et al. Multi-functional core-shell hybrid nanogels for pH-dependent magnetic manipulation, fluorescent pH-sensing, and drug delivery. Biomaterials 2011;32(36):9876–87. https://doi.org/10.1016/j.biomaterials.2011.08.082. PMid: 21944827.
[45] Wu W, Shen J, Banerjee P, et al. Core–shell hybrid nanogels for integration of optical temperature-sensing, targeted tumor cell imaging, and combined chemo-photothermal treatment. Biomaterials 2010;31(29):7555–66. https://doi.org/10.1016/j.biomaterials.2010.06.030. PMid: 2064348.
[46] Sánchez-Iglesias A, Grzelczak M, Rodríguez-González B, et al. Synthesis of multifunctional composite microgels *via in situ* Ni growth on pNIPAM-coated Au nanoparticles. ACS Nano 2009;3(10):3184–90. https://doi.org/10.1021/nn9006169. PMid: 19769339.
[47] Begines B, Ortiz T, Pérez-Aranda M, et al. Polymeric nanoparticles for drug delivery: Recent developments and future prospects. Nanomaterials 2020;10 (7):1403. https://doi.org/10.3390/nano10071403. PMid: 32707641.
[48] Romero MP, Marangoni VS, de Faria CG, et al. Graphene oxide mediated broad-spectrum antibacterial based on bimodal action of photodynamic and photothermal effects. Front Microbiol 2020;10:2995. https://doi.org/10.3389/fmicb.2019.02995. PMid: 32010081.
[49] Dong X, Sun Z, Wang X, et al. An innovative MWCNTs/DOX/TC nanosystem for chemo-photothermal combination therapy of cancer. Nanomedicine 2017;13 (7):2271–80. https://doi.org/10.1016/j.nano.2017.07.002.
[50] Lim JH, Kim DE, Kim E-J, et al. Functional graphene oxide-based nanosheets for photothermal therapy. Macromol Res 2018;26(6):557–65. https://doi.org/10.1007/s13233-018-6067-3. PMid: 32062387.
[51] Tager AA, Safronov AP, Sharina SV, et al. Thermodynamic study of poly(N-vinyl caprolactam) hydration at temperatures close to lower critical solution temperature. Colloid Polym Sci 1993;271(9):868–72. https://doi.org/10.1007/BF00652769.
[52] Kou Y, Wang S, Luo J, et al. Thermal analysis and heat capacity study of polyethylene glycol (PEG) phase change materials for thermal energy storage applications. J Chem Thermodyn 2019;128:259–74. https://doi.org/10.1016/j.jct.2018.08.031.
[53] Grössinger R. Correlation between the inhomogeneity and the magnetic anisotropy in polycrystalline ferromagnetic materials. J Magn Magn Mater 1982;28(1–2):137–42. https://doi.org/10.1016/0304-8853(82)90037-3.
[54] Batlle X, García del Muro M, Tejada J, et al. Magnetic study of *M*-type doped barium ferrite nanocrystalline powders. J Appl Phys 1993;74(5):3333–40. https://doi.org/10.1063/1.354558.
[55] Kodama RH. Magnetic nanoparticles. J Magn Magn Mater 1999;200(1–3):359–72. https://doi.org/10.1016/S0304-8853(99)00347-9.
[56] Zhang D, Klabunde K, Sorensen C, et al. Magnetization temperature dependence in iron nanoparticles. Phys Rev B Condens Matter Mater Phys 1998;58(21):14167–70. https://doi.org/10.1103/PHYSREVB.58.14167.
[57] Xiao G, Chien CL. Temperature dependence of spontaneous magnetization of ultrafine Fe particles in Fe-$SiO_2$ granular solids. J Appl Phys 1987;61 (8):3308–10. https://doi.org/10.1063/1.338891.
[58] Cao XT, Showkat AM, Kang I, et al. $\beta$ -cyclodextrin multi-conjugated magnetic graphene oxide as a nano-adsorbent for methylene blue removal. J Nanosci Nanotechnol 2016;16(2):1521–5. https://doi.org/10.1166/jnn.2016.11987. PMid: 27433613.
[59] Amiri A, Baghayeri M, Sedighi M. Magnetic solid-phase extraction of polycyclic aromatic hydrocarbons using a graphene oxide/$Fe_3O_4$@polystyrene nanocomposite. Microchim Acta 2018;185(8):1–9. https://doi.org/10.1007/s00604-018-2928-x.
[60] Mahdavi M, Ahmad MB, Haron MJ, et al. Synthesis, surface modification and characterisation of biocompatible magnetic iron oxide nanoparticles for biomedical applications. Molecules 2013;18(7):7533–48. https://doi.org/10.3390/molecules18077533. PMid: 23807578.
[61] Donadel K, Felisberto MDV, Fávere VT, et al. Synthesis and characterization of the iron oxide magnetic particles coated with chitosan biopolymer. Mater Sci Eng C 2008;28(4):509–14. https://doi.org/10.1016/j.msec.2007.06.004.
[62] Qu J, Liu G, Wang Y, et al. Preparation of $Fe_3O_4$–chitosan nanoparticles used for hyperthermia. Adv Powder Technol 2010;21(4):461–7. https://doi.org/10.1016/j.apt.2010.01.008.
[63] Huang P, Lin J, Yang D, et al. Photosensitizer-loaded dendrimer-modified multi-walled carbon nanotubes for photodynamic therapy. J Control Release 2011;152(supp 1):e33–4. https://doi.org/10.1016/j.jconrel.2011.08.105. PMid: 22195908.
[64] Xiao D, Qi H, Teng Y, et al. Advances and challenges of fluorescent nanomaterials for synthesis and biomedical applications. Nanoscale Res Lett 2021;16(1):167. https://doi.org/10.1186/s11671-021-03613-z. PMid: 34837561.
[65] Ren Y, Liu H, Liu X, et al. Photoresponsive materials for antibacterial applications. Cell Rep Phys Sci 2020;1(11):. https://doi.org/10.1016/J.XCRP.2020.100245100245.
[66] Huo J, Jia Q, Huang H, et al. Emerging photothermal-derived multimodal synergistic therapy in combating bacterial infections. Chem Soc Rev 2021;50 (15):8762–89. https://doi.org/10.1039/D1CS00074H. PMid: 34159993.
[67] Liu Z, Zhao X, Yu B, et al. Rough carbon–iron oxide nanohybrids for near-infrared-II light-responsive synergistic antibacterial therapy. ACS Nano 2021;15(4):7482–90. https://doi.org/10.1021/acsnano.1c00894. PMid: 3385619.
[68] Mei L, Shi Y, Cao F, et al. PEGylated phthalocyanine-functionalized graphene oxide with ultrahigh-efficient photothermal performance for triple-mode antibacterial therapy. ACS Biomater Sci Eng 2021;7(6):2638–48. https://doi.org/10.1021/acsbiomaterials.1c00178. PMid: 33938721.
[69] Xu JW, Yao K, Xu ZK. Nanomaterials with a photothermal effect for antibacterial activities: An overview. Nanoscale 2019;11(18):8680–91. https://doi.org/10.1039/C9NR01833F. PMid: 31012895.
[70] Hand JW, ter Haar G. Heating techniques in hyperthermia. Br J Radiol 1981;54 (642):443–66. https://doi.org/10.1259/0007-1285-54-642-443. PMid:7016236.
[71] Hergt R, Dutz S, Müller R, et al. Magnetic particle hyperthermia: Nanoparticle magnetism and materials development for cancer therapy. J Phys Condens Matter 2006;18(38):S2919–34. https://doi.org/10.1088/0953-8984/18/38/S26.
[72] Zhang L, Hou L, Zhang S, et al. Mechanism of *S. aureus* ATCC 25923 in response to heat stress under different water activity and heating rates. Food Control 2020;108:106837. https://doi.org/10.1016/j.foodcont.2019.106837.
[73] Lagos K.J., Buzzá H.H., Bagnato V.S., et al. Carbon-based materials in photodynamic and photothermal therapies applied to tumor destruction. Int J Mol Sci 2021;23(1):22. doi:10.3390/ijms23010022. PMid: 35008458.
[74] Mroz P, Yaroslavsky A, Kharkwal GB, et al. Cell death pathways in photodynamic therapy of cancer. Cancers 2011;3(2):2516–39. https://doi.org/10.3390/cancers3022516. PMid: 23914299.
[75] Marangon I, Ménard-Moyon C, Silva AKA, et al. Synergic mechanisms of photothermal and photodynamic therapies mediated by photosensitizer/carbon nanotube complexes. Carbon 2016;97:110–23. https://doi.org/10.1016/j.carbon.2015.08.023.
[76] Naserzadeh P, Ansari Esfeh F, Kaviani M, et al. Single-walled carbon nanotube, multi-walled carbon nanotube and $Fe_2O_3$ nanoparticles induced mitochondria mediated apoptosis in melanoma cells. Cutan Ocul Toxicol 2018;37 (2):157–66. https://doi.org/10.1080/15569527.2017.1363227. PMid: 28768445.
[77] Dias LD, Buzzá HH, Stringasci MD, et al. Recent advances in combined photothermal and photodynamic therapies against cancer using carbon nanomaterial platforms for *in vivo* studies. Photochem 2021;1(3):434–47. https://doi.org/10.3390/PHOTOCHEM1030026.
[78] Liu Z, Davis C, Cai W, et al. Circulation and long-term fate of functionalized, biocompatible single-walled carbon nanotubes in mice probed by Raman spectroscopy. Proc Natl Acad Sci 2008;105(5):1410–5. https://doi.org/10.1073/pnas.0707654105. PMid: 18230737.